ELSEVIER

Journal of Nuclear Materials 245 (1997) 161–168

journal of nuclear materials

Microstructural characterization of the stabilized fluorite phases formed in the $Ca_{1-y}La_yU_2O_{6+x}$ $(0 \leq y \leq 0.8)$ system.

E. Gómez-Rebollo, P. Herrero, R.M. Rojas *

Instituto de Ciencia de Materiales de Madrid, CSIC, Cantoblanco, 28049 Madrid, Spain

Received 15 August 1996; accepted 11 February 1997

Abstract

The thermal behaviour and stability of the fluorite structure in the $Ca_{1-y}La_yU_2O_{6+x}$ $(0 \leq y \leq 0.8)$ system during ageing have been studied by thermal analysis and X-ray powder diffraction. When the amount of La^{3+} incorporated into the $Ca_{1-y}La_yU_2O_{6+x}$ structure is ≥ 0.6 the complete stabilization of the fluorite phase is achieved. This phase remains stable over the temperature range from room temperature–1400°C even after being submitted to long term give time. For lower amounts of La^{3+} a mixture of cubic fluorite and calcium lanthanum diuranate solid solution is obtained on annealing. The microstructural characterization carried out by electron diffraction and high resolution transmission electron microscopy reveals short range order for the high temperature quenched materials. Annealing of the oxides leads to the formation of ordered nanodomains embedded within the fluorite matrix, but no ordered single phase is isolated. A hexagonal cell of $a_H = 3.8$ and $c_H = 18.8$ Å has been deduced for the domains.

1. Introduction

During fission of uranium in a nuclear reactor a large number of fission products such as Cs, Sr, Ba, La, etc. are formed. They can be accommodated into the UO_2 structure by forming solid solutions in substitution for uranium in the cation sublattice. Alkaline, alkaline-earth and some lanthanide ions have been reported to form uranates with many different stoichiometries and crystal structures, that can stabilize uranium dioxide against volatilization in an oxidizing atmosphere [1,2]. Many of these uranium mixed-oxides crystallize with the disordered fluorite-type structure, of which the systems $UO_{2\pm x}$–R_2O_3 (R = Ln, Y, Sc) are particularly notable for their extensive formation of non-stoichiometric fluorite-type phases [3,4]. The formation in oxidizing conditions of a fluorite-type phase with alkaline-earth cations has also been reported, its stability being limited to the higher temperature region ($T > 1200$°C) [5]. Annealing of fluorite-type materials yields ordered phases, the structure of which can be described in terms of superstructures of the basic fluorite cell [6–10]. The structural changes caused by the 'ageing' phenomena are related to the ordering processes which cause in many cases, variation of the physico-chemical properties of the original materials.

The progressive substitution of calcium for lanthanum in calcium diuranate CaU_2O_7 leads to the formation of a stabilized fluorite-type material [11]. However, the evolution of the lanthanum-doped uranates versus annealing has not been studied. Accordingly, the aim of this work is to better characterize the U–Ca–La–O system and amplify previous results [11]. Therefore, a detailed study of the effects of annealing on the lanthanum-doped CaU_2O_7, has been undertaken.

2. Experimental

Materials with the general composition $Ca_{1-y}La_yU_2O_{6+x}$ $(0 \leq y \leq 0.8)$, that can also be expressed as $Ca_{0.33-y}La_yU_{0.67}O_{2+x}$ $(0 \leq y \leq 0.27)$, were prepared from stoichiometric amounts of calcium carbonate $CaCO_3$ (Merck reagent grade), uranium oxide UO_3

* Corresponding author. Tel.: +34-1 334 9000; fax: +34-1 372 0623.

PII S0022-3115(97)00013-5

(supplied by the Centro de Investigaciones Energeticas, Medioambientales y Tecnológicas (CIEMAT), formerly JEN, Junta de Energía Nuclear) and lanthanum uranyl propionate $LaUO_2(C_2H_5COO)_5 \cdot 3H_2O$. A previous characterization of the CIEMAT uranium oxide had to be undertaken since chemical specifications for this material were not available. The X-ray diffraction pattern of the raw oxide (Fig. 1a) indicated a mixture of two crystalline phases: $UO_3.0.8H_2O$ [10-309 JCPDS file] and γ'-UO_3 [31-1423 JCPDS-file] (Fig. 1b, c). The infrared spectrum of the original material (Fig. 2), showed three bands at 1390 (s), 1030 (m) and 730 (w) cm^{-1} that were assigned to the $\nu_3(NO_2)_s$, $\nu_1(NO)_s$ and $\nu_4(NO_2)_\delta$ fundamental modes of the nitrate ion [12,13]. These bands are observed in the I.R. spectrum of $UO_2(NO_3)_2.6H_2O$ [14] and indicate that this salt is present as an impurity due to the procedure followed for the synthesis of the supplied uranium oxide. Corresponding DTA and TG curves are shown in Fig. 3. The weight loss observed up to $\approx$ 425°C (4.5%) is caused by the loss of water and nitrate groups yielding β-UO_3, which exothermally transforms to γ'-UO_3 at $\approx$ 500°C. Between 650 and 710°C the decomposition reaction γ'-$UO_3 \rightarrow 1/3\ U_3O_8$ takes place [15]. According to these results the original uranium oxide was heated at 500°C for 24 h prior to being used for the preparation of the samples and the corresponding X-ray pattern is shown in Fig. 1d. $LaUO_2(C_2H_5COO)_5 \cdot 3H_2O$ was obtained by the procedure described elsewhere [16,17].

Microcrystalline samples of the ternary oxides were prepared by a ceramic/organic precursor method. Appropriate amounts of the starting materials, $CaCO_3$, γ'-UO_3 and $LaUO_2(C_2H_5COO)_5 \cdot 3H_2O$ were intimately mixed by grinding in an agate mortar. The mixtures, after being pyrolized at 750°C, were calcined at 1400°C in air for 20 h in platinum containers. Samples were then quenched in air. Materials thus obtained were submitted to the non-accumulative thermal treatments indicated in Table 1. Samples annealed at 1300 and 900°C were quenched in air. Materials annealed at 500°C were allowed to cool slowly to room temperature. Specimens were obtained as black microcrystalline powders.

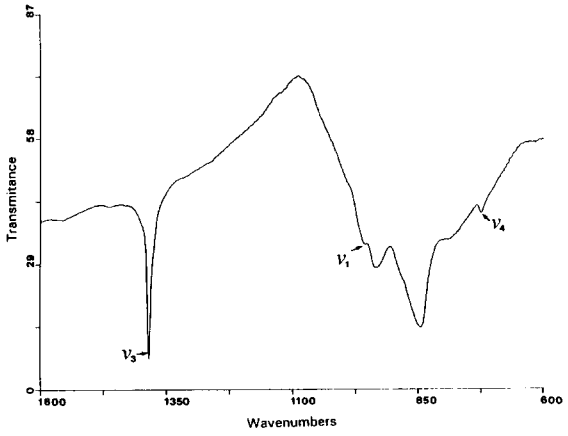

Fig. 2. Infrared spectra of uranium trioxide as supplied (s = strong, m = medium, w = weak).

X-ray powder diffraction patterns were recorded on a Siemens D-500 diffractometer with monochromatized Cu Kα radiation and W was used as an internal standard. Patterns were scanned at 1° 2θ min^{-1} and data were refined by a routine least-squares procedure. Uranium and lanthanum were determined using an ICP (inductive coupled plasma) method with a Perkin–Elmer Plasma 40 emission spectrometer; calcium was analyzed with a Pye Unicam SP9 atomic absorption spectrophotometer. Oxygen content was determined by a back-cerimetric titration method [18,19]. Chemical determination of uranium, lanthanum and calcium indicates that there was no appreciable volatilization of these elements during sample preparation. The oxygen content determination carried out for single phase materials shows that they all contain excess

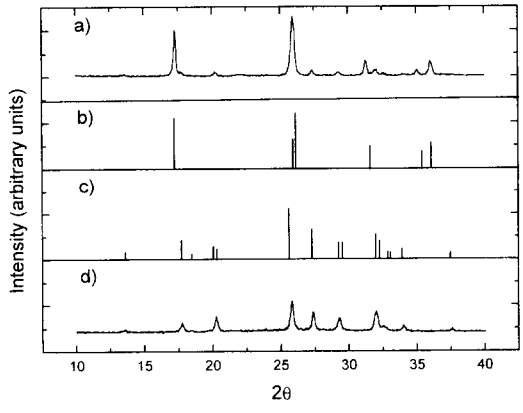

Fig. 1. X-ray patterns of uranium trioxide: (a) as supplied; (b) $UO_3 \cdot 0 \cdot 8H_2O$ [10-309 JCPDS file]; (c) γ'-UO_3 [31-1423 JCPDS file]; (d) after heating at 500°C for 24 h.

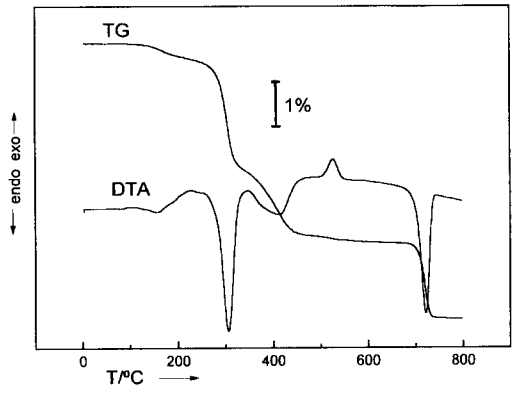

Fig. 3. Differential thermal analysis (DTA) and thermogravimetric (TG) curves of uranium trioxide as supplied.

Table 1
Nominal composition, thermal treatments, phases obtained and cubic cell parameters for $Ca_{1-y}La_yU_2O_{6+x}$ ($0 \le y \le 0.8$) fluorite-type materials.

Composition	Temperature (°C)	Time (h)	Phases obtained	Cell parameters (Å)
$y = 0$, CaU_2O_{6+x}	1400	12	fluorite	5.371(3) [a]
	1400	20	fluorite	
	1300	100	fluorite	5.3709(6)
	900	100	CaU_2O_7	–
$y = 0.2$, $Ca_{0.8}La_{0.2}U_2O_{6+x}$	1400	12	fluorite	5.394(3) [a]
	1400	20	fluorite	
	1300	100	fluorite	5.3991(8)
	900	100	$(Ca, La)U_2O_7$	–
$y = 0.4$, $Ca_{0.6}La_{0.4}U_2O_{6+x}$	1400	12	fluorite	5.414(2) [a]
	1400	20	fluorite	
	1300	100	fluorite	5.4175(6)
	900	100	fluorite + $(Ca, La)U_2O_7$ [b]	5.422(2)
$y = 0.6$, $Ca_{0.4}La_{0.6}U_2O_{6+x}$	1400	12	fluorite	5.437(7) [a]
	1400	20	fluorite	
	1300	100	fluorite	5.439(4)
	900	100	fluorite	5.436(8)
	500 [c]	150	fluorite	5.456(5)
$y = 0.8$, $Ca_{0.2}La_{0.8}U_2O_{6+x}$	1400	12	fluorite	5.457(4) [a]
	1400	20	fluorite	
	1300	100	fluorite	5.462(2)
	900	100	fluorite	5.460(5)
	500 [c]	150	fluorite	5.483(2)

[a] From Ref. [11].
[b] Traces.
[c] Samples slowly cooled to room temperature. All other samples were quenched from the temperatures indicated.

oxygen (see Table 3). Thermal stability was investigated by using a simultaneous DTA/TG Stanton STA 781 instrument. DTA/TG curves were recorded for materials $0 \le y \le 0.8$ quenched from 1300°C. Runs were carried out at 10°C min^{-1} heating/cooling rate in still air up to 1350°C. About 60 mg of sample was used and α-Al_2O_3 was the inert reference. Transmission electron microscopy studies were made with an electron microscope JEOL 2000 FX II operated at 200 kV and fitted with a double tilting goniometer stage of $\pm 45°$. High resolution images were obtained with a JEOL 4000 CX operating at 400 kV. Specimens for study were crushed and dispersed in acetone and then transferred to holey carbon-coated copper grids.

3. Results and discussion

3.1. X-ray powder diffraction and thermal stability

Composition, thermal treatment and phases identified from X-ray powder diffraction are summarized in Table 1. All materials quenched from 1400 and 1300°C crystallized with the fluorite-type structure (space group *Fm3m*) with cell parameters in good agreement with those already reported for samples heated for 12 h at 1400°C and then quenched [11]. The cubic cell parameter increases linearly with y, and this effect is attributed to the larger ionic radii of $^{VIII}La^{3+}$ (1.16 Å) versus $^{VIII}Ca^{2+}$ (1.12 Å) ions [20].

Depending on the thermal behaviour of the specimens versus dynamical heating/cooling processes, the oxides can be placed into two groups: the first consists of samples $y = 0$ and 0.2; the second, all other compositions, $0.4 \le y \le 0.8$. DTA curves recorded for materials belonging to the first group show exo- and endothermic effects associated with weight variations (Fig. 4a, b). The samples exothermally oxidized at 800°C with a weight gain of $\approx 2.36\%$ and 2.34% for $y = 0$ and 0.2, respectively, give way to the formation of the almost fully oxidized materials (Table 2). Secondly, the endothermic effects observed at ≈ 1000°C are assigned to the reversible reduction reaction. Removal of oxygen occurred at this temperature and materials recovered their initial stoichiometries. Finally, the reversible oxidation process that takes place on cooling shows, in both cases, a significant hysteresis; exothermic maxima are shifted between ≈ 250 and 300°C towards higher temperatures than those recorded for the first oxidation reaction that takes place on heating.

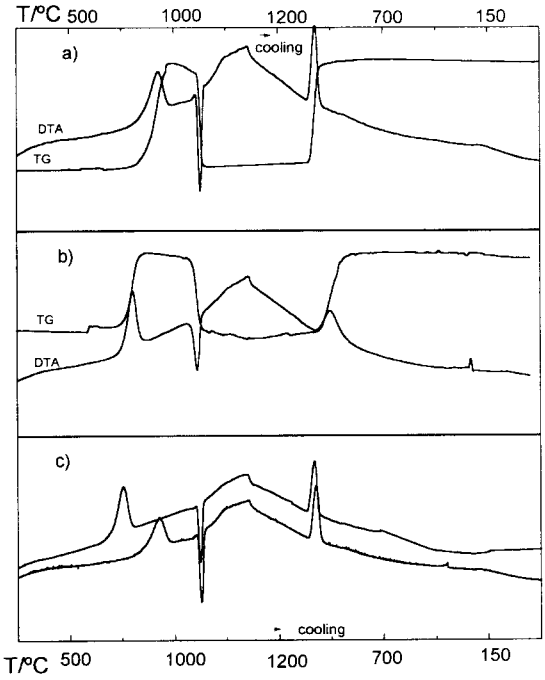

Fig. 4. DTA and TG curves of: (a) $y = 0$; (b) $y = 0.2$; (c) DTA and TG curves recorded for two different batches of the $y = 0$ specimen.

The thermal stability of the compound $y = 0.2$ agrees with previous data [11]; however, significant differences are observed in the case of the undoped calcium diuranate ($y = 0$). On the one hand, Cordfunke et al. [21] pointed out that the reversible oxidation ⇄ reduction reactions take place at the same temperature, 1075°C. On the other hand, we have reported [11] that the first oxidation reaction occurred in two consecutive steps at lower temperatures than those determined here. To investigate these discrepancies, we proceeded to record thermograms for three different batches of the $y = 0$ material quenched from 1300°C and two of them are presented in Fig. 4c. The onset of the first exothermic oxidation peak ranges within a ≈ 150°C interval (from 665 to 804°C), while the temperature for the following endo- and exothermic effects remained almost invariant. Temperatures and experimental weight variations for the three measured batches are summarized in Table 2. These data show that the first exothermic reaction takes place over a broad temperature range and differences between thermograms recorded for the samples quenched from 1400° (12 h) or 1300°C could arise from the different thermal treatments to which the samples were originally submitted. However we have not been able to provide a reliable explanation for this behaviour. Moreover, residues of thermal analysis for both $y = 0$ and 0.2 show X-ray patterns similar to CaU_2O_7 [21-168 JCPDS file] [22] and maxima of a fluorite-type material are not observed, as was previously reported [11]. The cooling process, that in this work has been carried out at a controlled cooling rate, avoids quenching of the sample. If materials are allowed to cool freely within the furnace of the thermal analyzer as it was previously done [11], partial quenching of the sample occurs.

For compositions $0.4 \leq y \leq 0.8$, neither significant weight variations in TG curves nor any thermal effects were observed in DTA traces. These results agree with previous work [11].

In order to confirm the long-term stability of materials, batches of each composition were annealed at the temperatures and periods shown in Table 1. At 900°C, sample

Table 2
Temperatures and mass variation for $Ca_{1-y}La_yU_2O_{6+x}$ ($y = 0$, 0.2) compounds determined from thermal analysis.

Sample [a] $Ca_{1-y}La_yU_2O_{6+x}$	Temperature of the peaks (°C)			Weight variation (%)	Reaction
	T_i	T_{max}	T_f		
$y = 0$, $CaU_2O_{6.06}$					
(a)	665	743	795	+2.39	*exothermal* $CaU_2O_{6.06}$ (fcc-type) → $CaU_2O_{6.96}$
(b)	721	781	825	+2.37	
(c)	804	912	976	+2.34	
(a)	1095	1113	1140	−2.34	*endothermal* $CaU_2O_{6.96}$ → $CaU_2O_{6.06}$ (fcc-type)
(b)	1096	1115	1144	−2.35	
(c)	1096	1119	1145	−2.35	
(a)	1054	1015	984	+2.30	*exothermal* $CaU_2O_{6.06}$ (fcc-type) → $CaU_2O_{6.96}$
(b)	1052	1017	987	+2.38	
(c)	1054	1010	969	+2.34	
$y = 0.2$, $Ca_{0.8}La_{0.2}U_2O_{6.07}$					
	708	787	844	+2.34	$Ca_{0.8}La_{0.2}U_2O_{6.07}$ (fcc-type) → $Ca_{0.8}La_{0.2}U_2O_{6.98}$
	1046	1097	1133	−2.37	(fcc-type) $Ca_{0.8}La_{0.2}U_2O_{6.07}$
	1012	943	840	+2.36	$Ca_{0.8}La_{0.2}U_2O_{7.00}$

[a] Starting oxygen stoichiometry deduced from cerimetric back titration.
(a), (b) and (c) indicate different batches of the $y = 0$ sample.

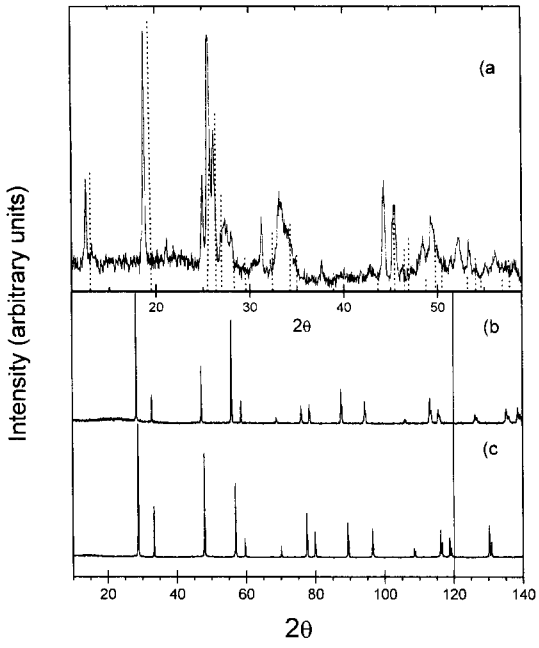

Fig. 5. X-ray patterns of samples: (a) $y = 0.2$ slowly cooled from 1200°C, (dotted lines correspond to CaU_2O_7 diffraction data from Ref. [22]]); (b) $y = 0.8$ annealed at 500°C for 150 h; (c) $y = 0$ quenched from 1300°C.

$y = 0.2$ follows the same behaviour as CaU_2O_6 ($y = 0$), which oxidizes to CaU_2O_7 at $T < 1100$°C. The X-ray pattern of the $y = 0.2$ sample (Fig. 5a) is similar to CaU_2O_7 but with diffraction maxima shifted towards lower 2θ angles. This suggests the formation of a mixed calcium lanthanum diuranate (Ca, La)U_2O_7 that, to the best of our knowledge, has never been reported. For $y = 0.4$, the X-ray pattern corresponds to a mixture of (Ca, La)U_2O_7 and a fluorite-type material, the latter being the major component. X-ray patterns for samples $y = 0.6$ and 0.8 annealed at 900 and 500°C (Fig. 5b) only showed maxima consistent with *Fm3m* of the fluorite structure, but shifted to higher 2θ angles with respect to the $y = 0$ composition (Fig. 5c). This indicates that materials $0.6 \leq y \leq 0.8$ are fully stabilized in the fluorite-type structure over the whole

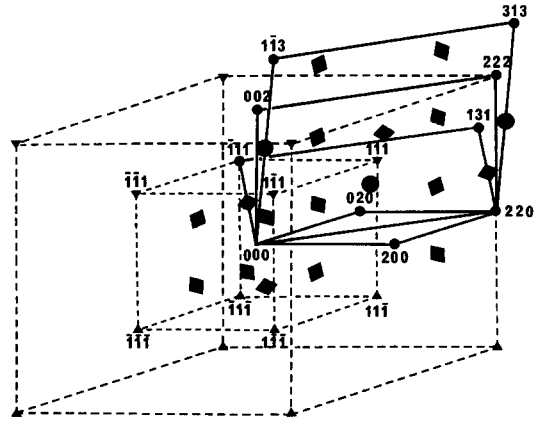

Fig. 7. Reciprocal lattice of the fluorite cell showing the position of the diffuse scattering as deduced from patterns shown in Fig. 6.

range of temperatures studied, even after being submitted to long annealing processes (150 h at 500°C).

Table 3 summarizes compositions deduced from chemical analysis, oxygen hyperstoichiometry and calculated mean uranium valence. All materials contain excess oxygen, becoming more significant as the lanthanum content increases. Annealing processes result in a slight increase of the oxygen hyperstoichiometry. Note that the calculated oxidation state of uranium is nearly 5^+ in the whole compositional range, the electroneutrality of this system being kept by the variation in the amount of oxygen, instead of by reduction of the uranium 5^+. This value has been found in several compounds such as the perovskite-type oxides MUO_3 (M = Li, Na, K and Rb)[23], $Ba_3CaU_2O_9$ and $Ba_3SrU_2O_9$ [24], in fluorite-type oxides $U_{1-y}La_yO_{2\pm x}$ [25], MgU_2O_6 and SrU_2O_6 [26] and more recently in CoU_2O_6 and NiU_2O_6 [27].

3.2. Electron diffraction and microscopy

The microstructure of these materials was determined by transmission electron microscopy. Electron diffraction patterns for samples synthesized at high temperature (1400

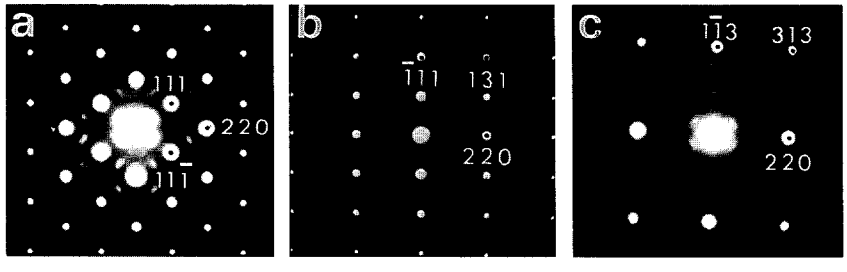

Fig. 6. Electron diffraction patterns of sample $y = 0$ quenched from 1300°C.

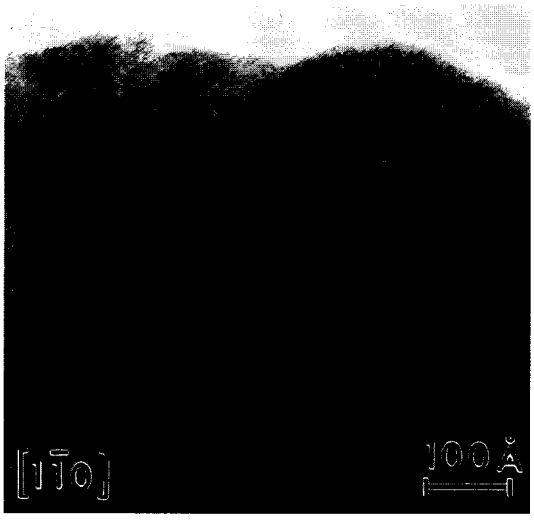

Fig. 8. Direct image corresponding to the pattern of Fig. 6a. Zone axis [1$\bar{1}$0].

and 1300°C) show a set of strong Bragg diffraction maxima corresponding to the reciprocal lattice of the fluorite cell, as well as some diffuse maxima. Some significant zone axes corresponding to the sample $y = 0$ are presented in Fig. 6. A schematic representation of the reciprocal cell is shown in Fig. 7. The presence of diffuse scattering indicates that quenched materials are in a high temperature short range order (SRO) state. This is reflected in the real image of Fig. 8 in which an 'orange-peel' like texture characteristic of these materials is shown.

Annealing at 900°C results, in some cases, in a transformation of the diffuse maxima into sharp spots, as can be

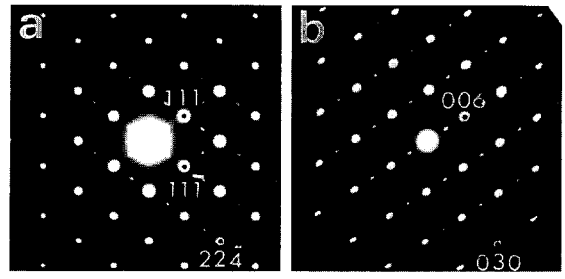

Fig. 9. Electron diffraction patterns along [1$\bar{1}$0]: (a) sample $y = 0.6$ annealed; (b) R_{III} phase formed in the $U_{1-y}La_yO_{2\pm x}$ system for $0.56 \leq y \leq 0.67$.

seen in Fig. 9a. Corresponding high resolution images of the sample $y = 0.6$ indicate a biphasic texture with well defined nanodomains of an ordered secondary phase embedded within the fluorite matrix (Fig. 10a). In Fig. 10b an enlarged area of the same image is shown.

A careful review of some related systems has revealed the existence of evident analogies with electron diffraction patterns and structural images of the R_{III} phase formed in the $U_{1-y}La_yO_{2\pm x}$ system in the compositional range $0.56 \leq y \leq 0.67$ [28]. Fig. 9b shows an electron diffraction pattern, along the [110] zone axis corresponding to the hexagonal R_{III} phase. Similarities arising from patterns of Fig. 9 are evident, taking into account that Fig. 9a reflects the presence of twining, evidently derived from the pre-existent disorder in the fluorite phase. Assuming a hexagonal symmetry for the nanodomains, the following unit cell parameters $a_H = 3.8$ Å, $c_H = 18.8$ Å can be deduced. A projection of this hexagonal cell is indicated in the enlarged area of Fig. 10b.

Table 3
Oxygen hyperstoichiometry (x) and calculated mean uranium valence for the single phase $Ca_{1-y}La_yU_2O_{6+x}$ ($0 \leq y \leq 0.8$) quenched materials.

Composition	Phases obtained	Quenching temperature (°C)	Oxygen hyper-stoichiometry (x)	Mean uranium valence
$y = 0$	fluorite	1300	+0.06(5)	5.1
	CaU_2O_7	900	−0.01(2)	–
$y = 0.2$	fluorite	1300	+0.07(2)	5.0
	(Ca, La)U_2O_7	900	+0.10(1)	–
$y = 0.4$	fluorite	1300	+0.21(9)	5.0
	fluorite + (Ca, La)U_2O_7	900	–	–
$y = 0.6$	fluorite	1300	0.30(4)	5.0
	fluorite	900	0.40(3)	5.1
	fluorite	500 [a]	0.35(7)	5.1
$y = 0.8$	fluorite	1300	0.30(1)	4.9
	fluorite	900	0.43(2)	5.0
	fluorite	500 [a]	0.48(6)	5.1

[a] Slowly cooled to room temperature.

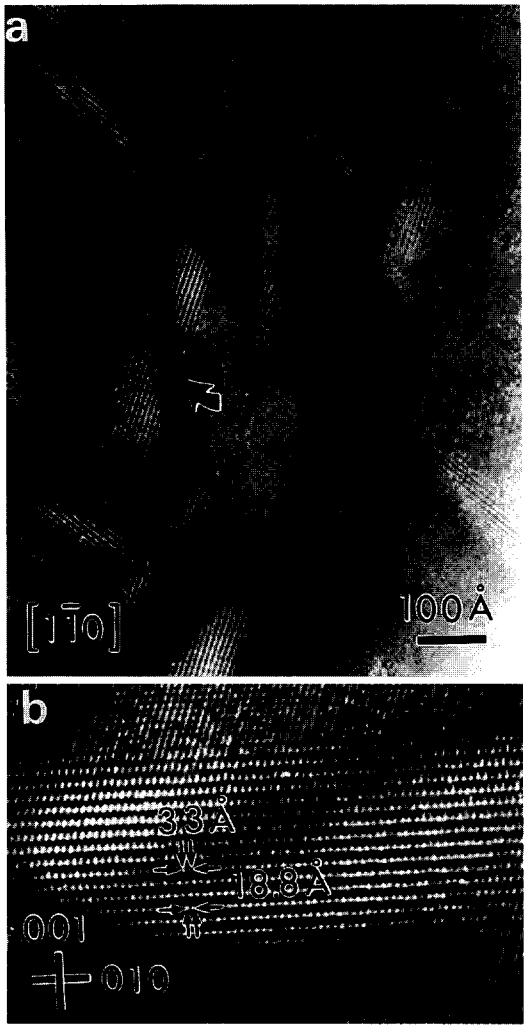

Fig. 10. HRTEM image corresponding to the ED pattern of Fig. 9a showing: (a) ordered nanodomains embedded within the fluorite matrix; (b) enlarged area of the zone indicated in (a). Fringes corresponding to the $d_{(010)}$ and $d_{(001)}$ of the proposed hexagonal unit cell are indicated.

Not all of the crystals examined show the presence of nanodomains and no ordered single phase could be isolated.

4. Concluding remarks

Only when the amount of La^{3+} ions incorporated into the $Ca_{1-y}La_yU_2O_{6+x}$ structure is ≥ 0.6 does the complete stabilization of the fluorite phase occur. This phase remains stable over the whole temperature range considered (room temperature–1400°C) even after long annealing times. For lower amounts of dopant (i.e., $y = 0.4$) and although DTA/TG curves did not show the existence of any transformation with temperature, annealing of this material yields a mixture of cubic fluorite and calcium lanthanum diuranate. All the materials synthesized had excess oxygen and the mean valence of uranium does not significantly change with the concentration of La^{3+}; only a small increase of the oxygen content on annealing is observed. This could be related to the existence of some U^{6+} in the annealed materials. In the high temperature fluorite-type oxides, a state of SRO has been detected. When annealed it transforms to ordered domains of several nanometers in extension and randomly distributed within the fluorite matrix. Since the formation of ordered nanodomains seems to be related to the amount of U^{6+} in the samples [28], the number of nanodomains is therefore limited and the average fluorite structure is preserved despite the presence of that domains.

Acknowledgements

The authors thank Mr A. García-Delgado for performance of the electron microscopy investigations and Mr R. Ropero for technical assistance. We also thank the Centro de Microscopía Electrónica de la Universidad Complutense de Madrid for facilities to use the JEOL 4000 EX microscope. This work has been supported by CICyT Projects MAT92-0202 and 95-0899.

References

[1] H. Kleykamp, J.O. Paschoal, R. Pejsa, F. Thommler, J. Nucl. Mater. 130 (1985) 426.
[2] R.W. Grimes, C.R.A. Catlow, Philos. Trans. R. Soc. London A335 (1991) 609.
[3] C. Keller, in: MTP International Review of Sciences, Inorganic Chemistry, Series 2, Vol. 7, ed. K. Bagnall (Butterworths, London, 1975) p. 10.
[4] D.J.M. Bevan, E. Summerville, in: Handbook on the Physics and Chemistry of Rare Earth, Vol. 3, eds. K.A. Gschneider Jr. and L. Eyring (North-Holland, Amsterdam, 1979) p. 401.
[5] T. Fujino, C. Miyake, in: Handbook on the Physics and Chemistry of the Actinides, Vol. 6, eds. A.J. Freeman and C. Keller (Elsevier, Amsterdam, 1991) p. 155.
[6] J.G. Allpress, H.J. Rossell, J. Solid State Chem. 15 (1975) 68.
[7] M.P. van Dijk, F.C. Milhoff, J. Burggraaf, J. Solid State Chem. 94 (1986) 377.
[8] R.L. Withers, J.G. Thomson, P.J. Barlow, J. Solid State Chem. 94 (1991) 89.
[9] P. García-Chain, R.M. Rojas, P. Herrero, J.R. Günter, J. Solid State Chem. 108 (1994) 236.
[10] R.M. Rojas, P. Herrero, P. García-Chain, J. Rodríguez-Carvajal, J. Solid State Chem. 112 (1994) 322.
[11] P. Herrero, R.M. Rojas, J. Solid State Chem. 73 (1988) 536.
[12] C.N.R. Rao, Chemical Applications of Infrared Spectroscopy (Academic Press, London, 1963) p. 351.
[13] G. Herzberg, Molecular Spectra and Molecular Structure: II:

Infrared and Raman Spectra of Polyatomic Molecules, 12th printing (van Nostrand, New Jersey, 1966) p. 178.
[14] G.L. Caldow, A.B. van Cleave, R.L. Eager, Can. J. Chem. 38 (1960) 772.
[15] P.C. Debets, Acta Crystallogr. 21 (1966) 589.
[16] Z.M. Alikhanova, G.V. Ellert, Russ. J. Inorg. Chem. 16 (1971) 63.
[17] R.M. Rojas, P. Herrero, F. Benetollo, G. Bombieri, J. Less-Common Met. 162 (1990) 105.
[18] S.R. Dharwadkar, M.S. Chandrasekharaiah, Anal. Chim. Acta 45 (1969) 545.
[19] T. Fujino, T. Yamashita, Fresenius Z. Anal. Chem. 314 (1983) 156.
[20] R.D. Shannon, Acta Crystallogr. A32 (1976) 751.
[21] E.H.P. Cordfunke, B.O. Loopstra, J. Inorg. Nucl. Chem. 29 (1967) 51.
[22] C. Brisi, M. Montorsi Appendino, Ann. Chim. Rome 59 (1969) 400.
[23] A.M. Chippindale, P.G. Dickens, W.T.A. Harrison, J. Solid State Chem. 78 (1989) 256.
[24] Y. Hintasu, J. Solid State Chem. 108 (1994) 356.
[25] P. Herrero, P. García-Chain, R.M. Rojas, J. Solid State Chem. 87 (1990) 331.
[26] C. Miyake, O. Kawasaki, K. Gotoh, A. Nakatami, J. Alloys Compounds 200 (1993) 187.
[27] Y. Hinatsu, J. Solid State Chem. 114 (1995) 595.
[28] R.M. Rojas, P. Herrero, P. García-Chain, J. Rodríguez-Carvajal, J. Solid State Chem. 112 (1994) 322.